

Binary Black Hole Accretion Flows From a Misaligned Circumbinary Disk

Kimitake HAYASAKI^{1,2}, Hideki SAITO^{2,3}, and Shin MINESHIGE²

¹*Korea Astronomy and Space Science Institute, Daedeokdaero 776, Yuseong, Daejeon 305-348, Korea*

²*Department of Astronomy, Kyoto University, Sakyo-ku, Kyoto 606-8502, Japan*

³*Nagano City Museum, Oshimadamachi, Nagano, Nagano 381-2212, Japan*

kimi@kasi.re.kr; kimi@kusastro.kyoto-u.ac.jp

(Received 2012 0; accepted 2012 0)

Abstract

We study the basic properties of accretion flows onto binary supermassive black holes, including the cases in which a circumbinary disk is misaligned with the binary orbital plane, by means of three-dimensional Smoothed Particle Hydrodynamics simulations. We find that a circular binary system with a misaligned circumbinary disk normally produces a double peaked mass-accretion-rate variation per binary orbit. This is because each black hole passes across the circumbinary disk plane and captures gas twice in one orbital period. Even in misaligned systems, however, a single peaked mass-accretion-rate variation per binary orbit is produced, if the orbital eccentricity is moderately large ($e \gtrsim 0.3$). The number of peaks in mass accretion rates can be understood simply in terms of the orbital phase dependence of the distance between each binary black hole and its closest inner edge of the circumbinary disk. In the cases of eccentric binary black holes having different masses, the less massive black hole can get closer to the circumbinary disk than the massive one, thus tidally splitting gas from its inner edge, but the created gas flows are comparably captured by both black holes with a short time delay. As a consequence, the combined light curve shows periodic occurrence of double-peaked flares with a short interval. This may account for the observed light variations of OJ287.

Key words: accretion, accretion disks — binary black holes — black hole physics — galaxies: nuclei

1. Introduction

Hierarchical structure formation scenario tells us that a galaxy grows by merger of smaller galaxies. The recently confirmed correlation between the mass of supermassive black holes (SMBHs) and the mass or luminosities of the bulge of their host galaxies strongly support the idea that SMBHs have grown with the growth of their host galaxies (Magorrian et al. 1998; Gebhardt et al. 2000; Ferrarese & Merritt 2000). These relationships suggest that each SMBH in the center of each galaxy should have evolved toward coalescence in a merged galaxy. If this is the case, a binary of SMBHs should be formed in a merged galactic nucleus before two black holes finally coalesce, yet no binary SMBHs have clearly been identified so far except for some candidates at large separations (\sim kpc) (e.g., Komossa et al. 2003).

The merger of two SMBHs processes via three stages (Begelman et al. 1980): First, each black hole sinks into a common center of a merged galactic nucleus by the dynamical friction with the surrounding field stars and gas (Escala et al. 2005; Dotti et al. 2007). When the separation between the two black holes becomes as short as one parsec or so, the dynamical friction is no longer efficient and a hard binary is formed (Mayer et al. 2007). The separation of such a hard binary should have been reduced by some unknown mechanism. When the separation becomes as short as one parsec or less, finally, the binary rapidly merge by emitting gravitational wave radiation to become a single SMBH. However, there has been many discussions about by what mechanism the binary orbit decays in the second stage. One of predominant candidates is the interaction between the binary and the circumbinary disk (Ivanov et al. 1999; Gould & Rix 2000; Armitage & Natarajan 2002; Hayasaki 2009; Haiman et al. 2009; Cuadra et al. 2009; Lodato et al. 2009; Hayasaki et al. 2010; Nixon et al. 2011a; Kocsis et al. 2012a; Kocsis et al. 2012b).

It is an observational challenge how to identify binary SMBHs on such a subparsec scale (see Komossa (2006) for a review). Several ways have been proposed: Periodic optical and radio outbursts (e.g., OJ 287) (Sillanpää et al. 1988; Valtonen et al. 2011), wiggled patterns of the radio jet, indicating precessional motions on a parsec scale (Yokosawa & Inoue 1985; Lovanov&Roland 2005), X-shaped morphology of radio lobes (Merritt&Ekers 2002), double-peaked broad emission lines in active galactic nuclei (AGNs) (Gaskell 1996) and distant quasars (Bogdanović et al. 2009; Dotti et al. 2009; Boroson & Lauer 2009; Montuori et al. 2011; Montuori et al. 2011; Eracleous et al. 2012), double compact cores with a flat radio spectrum (Rodriguez et al. 2006), orbital motion of the compact core with a periodic flux variation (Sudou et al. 2003; Iguchi & Sudou 2010), and so on.

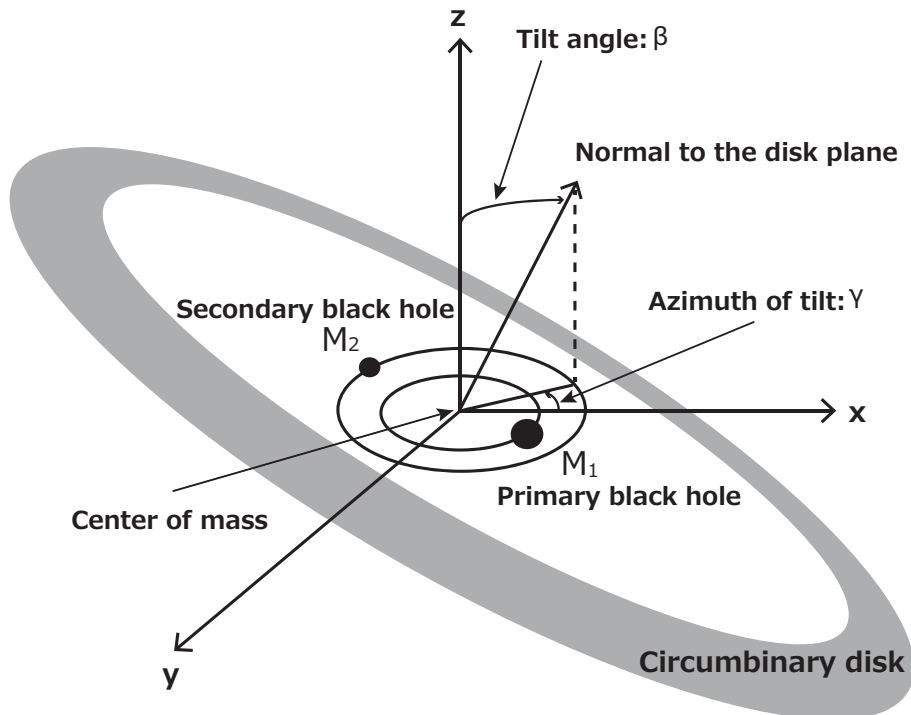


Fig. 1. Configuration of our model. There are two angles (β, γ) which specify the orientation of the circumbinary disk plane with respect to the binary orbital plane (x - y plane).

With successive discoveries of binary black hole candidates and ongoing constructions of advanced gravitational wave detectors such as *eLISA* (Amaro-Seoane et al. 2012), much attention has been recently paid to electromagnetic signatures from binary SMBH systems, such as afterglows (Milosavljević & Phinney 2005; Tanaka & Menou 2010; Tanaka et al. 2012), precursors (Chang et al. 2009; Bode et al. 2010; Hayasaki 2011; Farris et al. 2011; Farris et al. 2012; Bode et al. 2012), periodic emissions (Artymowicz & Lubow 1996; Lehto & Valtonen 1996; Hayasaki et al. 2007; Hayasaki et al. 2008; Bogdanović et al. 2008; MacFadyen & Milosavljević 2008; Roedig et al. 2011; Sesana et al. 2012; Shi et al. 2012; Noble et al. 2012; Daniel et al. 2012), and a dual-jet structure (Palenzuela et al. 2010; Mošta et al. 2010), in the context of a massive black hole coalescence. There are also several theoretical studies on the observational methodology to probe the presence of a gaseous disk around coalescing binary black holes through the waveform analyses of the emitted gravitational waves (Kocsis et al. 2011; Yunes et al. 2011; Hayasaki et al. 2012).

In most of the previous studies, it has been assumed that the circumbinary disk is aligned with the binary orbital plane. However, the angular momentum vector of the binary does not always coincide with that of the circumbinary disk because the circumbinary disk would be formed independently of the formation of binary SMBHs. Therefore, the orientation of a circumbinary disk plane can be taken arbitrarily with respect to the binary orbital plane. It has been shown quite recently that the circumbinary disk which rotates in such an opposite direction as the binary rotation can be stable, if the misalignment angle between the binary orbital plane and the initial circumbinary disk plane is more than $\pi/2$ (Nixon 2012), whereas the circumbinary disk which rotates in a prograde direction for the binary is stable, if the misalignment angle is less than $\pi/2$. However, accretion flows onto binary SMBHs around the misaligned circumbinary disk rotating in a prograde direction have been poorly investigated. The misalignment angle is expected to produce complex light variations which never appear otherwise. Especially, two periodic outbursts per orbital period may be obtained, since there are two epochs in one orbital period, when the distance between the binary and the inner edge of circumbinary disk is shortest. By contrast, the binary orbital eccentricity produces a single, steep peak per binary orbit in a coplanar system (Hayasaki et al. 2007; Roedig et al. 2011).

In this paper, we focus our study on basic properties of accretion flows onto binary SMBHs including the cases of a misaligned circumbinary disk. In the next section, we will describe our models and methods of calculations. The numerical results will be presented in section 3. In section 4, we provide a simple model in order to understand the numerical results. The final section is devoted to summary and discussion.

2. Our models and calculation methods

In this section, we first explain our models and next describe our calculation methods.

2.1. Initial settings

Figure 1 illustrates a schematic picture of the setting of our model; binary black holes rotating each other are surrounded by a misaligned circumbinary disk. The binary is put on the x - y plane with its center of mass being at the origin. The masses of the primary and secondary black holes are represented by M_1 and M_2 , respectively. We put a circumbinary disk around the origin. The unit vector of specific angular momentum of the circumbinary disk is expressed by (e.g. Pringle 1996)

$$\mathbf{j}_d = (\cos \gamma \sin \beta, \sin \gamma \sin \beta, \cos \beta), \quad (1)$$

where β is the tilt angle between the circumbinary disk plane and the binary orbital plane, and γ is the azimuth of tilt. The position vector of each black hole is given by

$$\mathbf{r}_i = (r_i \cos \phi, r_i \sin \phi, 0) \quad [i = 1, 2], \quad (2)$$

where

$$r_i = \eta_i \frac{a(1 - e^2)}{1 + e \cos \phi} \quad (3)$$

and ϕ is the true anomaly (hereafter, we regard the true anomaly as the orbital phase) (e.g., Murray & Dermott 1999), $\eta_1 \equiv q/(1 + q)$ and $\eta_2 \equiv 1/(1 + q)$ with binary mass ratio $q = M_2/M_1$, and $a = a_1 + a_2$ is the semi-major axis of the binary, where $a_1 \equiv \eta_1 a$ and $a_2 \equiv \eta_2 a$.

The circumbinary disk initially has a radially uniform density profile between the initial radius of the disk-inner edge, r_{ini} , and the radius of $r = r_{\text{ini}} + 0.05a$ (i.e., the initial width of the circumbinary disk is set to be $0.05a$). The material in the circumbinary disk rotates around the origin on the circular orbit with the Keplerian rotation velocity. The vertical density structure of the circumbinary disk is exponential; i.e., we assume a hydrostatic balance with constant temperature in the vertical direction. The initial mass of the circumbinary disk is $1.0 \times 10^{-4} M_\odot$. The disk temperature is assumed to be $T = 30700\text{K}$ everywhere. Note that this corresponds to the typical central temperature of a standard disk at $r = 2a$ around a single black hole with $10^8 M_\odot$ for a given mass input rate of $\dot{M}_{\text{inj}} = 1.0 M_\odot \text{ yr}^{-1}$ (Kato, Fukue & Mineshige 2008).

In Table 1, we summarize common model parameters for all models in the present study: total black hole mass ($M_1 + M_2$), semi-major axis of the binary orbit (a), initial mass of the circumbinary disk (M_{disk}), mass injection rate (\dot{M}_{inj}), disk temperature T_d , and Shakura-Sunyaev viscosity parameter α_{SS} (Shakura & Sunyaev 1973). The relation between α_{SS} and the SPH artificial viscosity parameters will be described in section 2.3. The binary orbital period, P_{orb} , is estimated to be approximately 9.4 yr by using the Keplerian third law.

Table 1. Common model parameters

Total black hole mass	$M_1 + M_2 = 10^8 M_\odot$
Semi-major axis	$a = 0.01 \text{ pc}$
(Orbital period)	$(P_{\text{orb}} = 2\pi a^{3/2} / \sqrt{G(M_1 + M_2)}) \approx 9.4 \text{ yr}$
Initial disk mass	$M_{\text{disk}} = 1.0 \times 10^{-4} M_\odot$
mass injection rate	$\dot{M}_{\text{inj}} = 1.0 M_\odot \text{ yr}^{-1}$
Disk temperature	$T_d = 30700 \text{ K}$
Disk viscosity	$\alpha_{\text{SS}} = 0.1$

2.2. Boundary conditions

Gas particles are added to the outer edge of the circumbinary disk from its outside in an arbitrary angles at a constant rate of $\dot{M}_{\text{inj}} = 1.0 M_\odot \text{ yr}^{-1}$. The inner edge of the circumbinary disk is determined by the balance between the tidal/resonant torque exerted by the binary black holes and the viscous torque of the circumbinary disk. We take an initial inner edge radius of the circumbinary disk to be $r_{\text{ini}} = 2.5$ for $e = 0.5$. In an equal-mass and circular binary, on the other hand, we take an initial inner edge radius as $r_{\text{ini}} = 1.68a$, corresponding to the tidal truncation radius where the tidal torque of the binary equals to the viscous torque of the circumbinary disk (Papaloizou & Pringle 1977; see also Table 1 of Artymowicz & Lubow 1994).

We set the outer calculation boundary at $r = 6.0a$, which is sufficiently far from the disk region so that the outer boundary should not affect the flow dynamics in the binary SMBH system. The SPH particles passing outward across the outer calculation boundaries are removed from the simulation box.

The accretion radius depends on the mass of each black hole. The black holes are modeled by sink particles with the fixed accretion radius of $r_{\text{acc}} = 0.1a$ or $0.05a$, depending on the black hole mass. Note that each accretion radius

is two orders of magnitude larger than the Schwarzschild radius of each black hole. Numerically, we remove all the particles that enter the region inside the accretion radius.

2.3. Numerical method

The simulations presented below are performed with the three-dimensional (3D) SPH code, which is based on a version originally developed by Benz 1990; Benz et al. 1990; Bate et al. 1995 and has been extensively used for various systems by many authors (e.g., Okazaki et al. 2002; Hayasaki et al. 2007; Okazaki et al. 2010; Takata et al. 2012). The SPH equations are composed of a mass conservation equation, a momentum equation with the SPH standard artificial viscosity, and an isothermal equation of state in substitution for an energy equation. These equations with the standard cubic-spline kernel are integrated using a second-order Runge-Kutta-Fehlberg integrator with individual time steps for each particle and a variable smoothing length (Bate et al. 1995), which results in saving enormous computational time when a large range of dynamical timescales are involved.

The artificial viscosity commonly used in SPH consists of two terms: a term that is linear in the velocity differences between particles, which produces a shear and bulk viscosity, and a term that is quadratic in the velocity differences, which is needed to eliminate particle interpenetration in high Mach number shocks. The parameters α_{SPH} and β_{SPH} control the linear and quadratic terms, respectively. In the simulations shown in this paper, the artificial viscosity is adjusted so as to keep the Shakura-Sunyaev viscosity parameter $\alpha_{\text{SS}} = 0.1$ (Shakura & Sunyaev 1973), using the approximate relation $\alpha_{\text{SS}} = 0.1 \alpha_{\text{SPH}} h/H$ and $\beta_{\text{SPH}} = 0$ (see Section 2.2 of Hayasaki et al. 2007), where h and H are the smoothing length of individual particles and the scale-height of the circumbinary disk, respectively.

Sink particles (i.e. black holes) are orbiting around each other, following the Keplerian third law, because perturbations by the interaction with SPH particles are negligible. In all models described in next subsection, total run time is 60 in a unit of P_{orb} , and the simulation time t is normalized by P_{orb} through this paper. The orbital phase is forwardly shifted by 0.03 at the end of run ($t = 60$) to correct the accumulation of numerical errors.

Table 2. Individual model parameters.

Model	$q \equiv M_2/M_1$	e	r_{in}/a	(β, γ)
A1	1.0	0.0	1.68	(0,0)
A2	1.0	0.0	1.68	$(\pi/6, \pi/2)$
A3	1.0	0.0	1.68	$(\pi/4, \pi/2)$
A4	1.0	0.0	1.68	$(\pi/6, 0)$
B1	1.0	0.5	2.50	(0,0)
B2	1.0	0.5	2.50	$(\pi/6, \pi/2)$
B3	1.0	0.5	2.50	$(\pi/4, \pi/2)$
B4	1.0	0.5	2.50	$(\pi/6, 0)$
C1	0.5	0.5	2.50	(0,0)
C2	0.5	0.5	2.50	$(\pi/6, \pi/2)$
C3	0.5	0.5	2.50	$(\pi/4, \pi/2)$

2.4. Calculated models

In the present study we are concerned with the observable quantities for various configurations of binary SMBHs with the circumbinary disk. Accordingly, we calculated eleven models, in total, by varying the binary mass ratio, binary orbital eccentricity, title angle, and azimuth of tilt. In Table 2, we summarize the model parameters: from the left to right, model number (first column), mass ratio of the secondary black hole to the primary one (second column), orbital eccentricity (third column), initial radius of the inner edge of the circumbinary disk in units of a (fourth column), and tilt angle and azimuth of tilt (β, γ) (fifth column, see Figure 1 and equation (1) for definitions of β and γ).

While Model A is an equal-mass and circular binary, Models B and C are eccentric binaries with equal black hole masses (Models B) and unequal black hole masses (Model C). Through this paper, we assign Model A2 as a fiducial model.

3. Accretion flows from a misaligned circumbinary disk to binary black holes

In this section, we examine how the basic properties of accretion flows onto each black hole depend on β , γ , e , and q , by performing 3D SPH simulations.

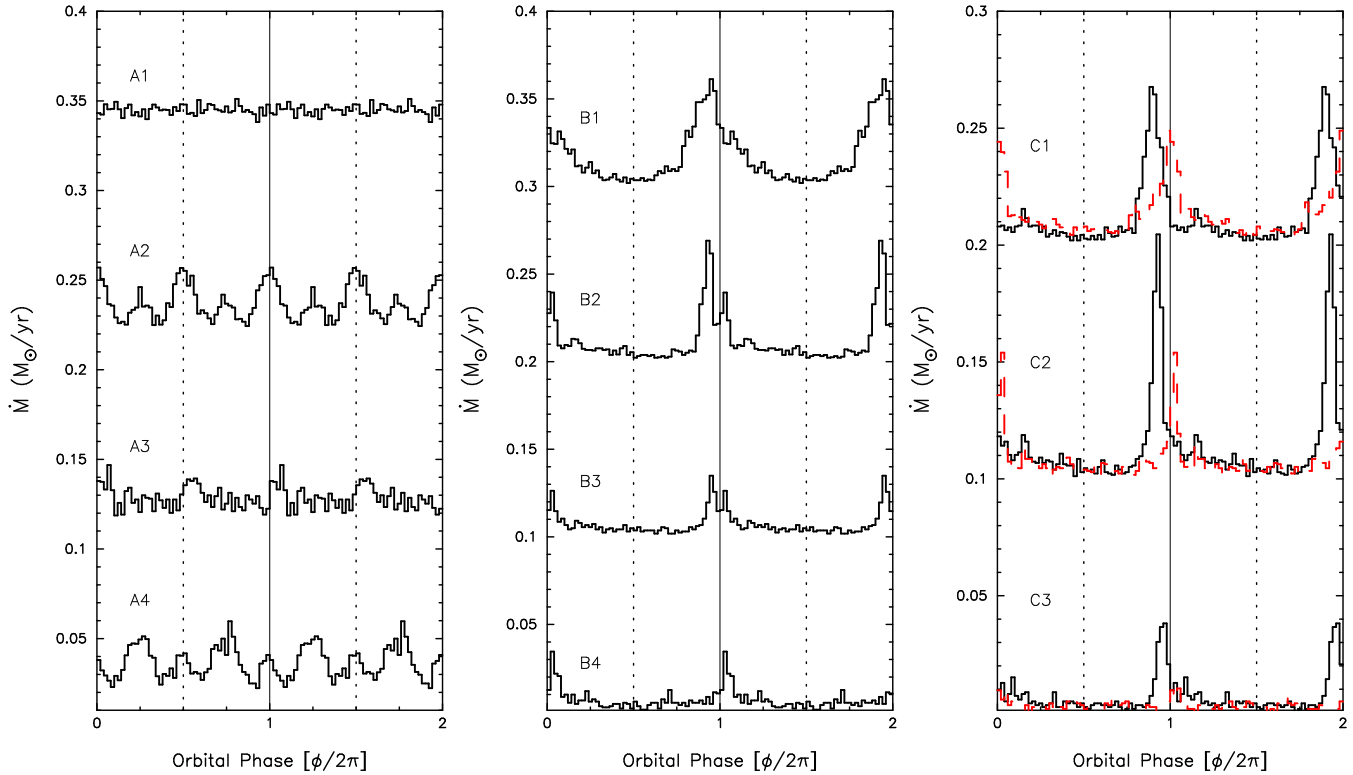


Fig. 2. Orbital phase dependence of mass accretion rates for all models. Models A1–A4, Models B1–B4, and Models C1–C3 are shown in the left panel, the middle panel, and the right panel, respectively. The data is folded on the orbital period over $40 \leq t \leq 60$. Here, we redefine the orbital phase in order that the phase 0 corresponds to the epoch of the periastron passage (see section 2.3). The binary black holes are at the periastron (or at the apastron) at phase 0.0 (0.5) for eccentric binaries (Models B1–C3). For clarity, we vertically offset the mass accretion rates for Model A1 and B1 by +0.3, for Models A2, B2, and C1 by +0.2, and for Models A3, B3, and C2 by +0.1 with respect to those of Models A4, B4, and C3, respectively. In the right panel, the solid line and dashed (red) line represent the mass accretion rates onto the primary black hole and that of the secondary one, respectively.

Table 3. Summary of averaged mass accretion rates, averaged circularization radii, and the number of SPH particles at the end of the run ($t=60$) for all models. Since the mass is injected to the circumbinary disk at the rate of $1M_{\odot}/\text{yr}^{-1}$, the averaged mass accretion rates indicate the fraction of the mass accretion rate onto each black hole to the mass injection rate.

Model @	$\langle \dot{M}_1 \rangle$ [$M_{\odot}\text{yr}^{-1}$]	$\langle \dot{M}_2 \rangle$ [$M_{\odot}\text{yr}^{-1}$]	$\langle r_{c,1} \rangle$ [a]	$\langle r_{c,2} \rangle$ [a]	N_{SPH}
A1	0.045	0.045	0.033	0.033	62157
A2	0.037	0.036	0.062	0.062	67774
A3	0.028	0.028	0.055	0.056	53866
A4	0.037	0.037	0.063	0.063	81149
B1	0.018	0.017	0.038	0.034	61022
B2	0.012	0.012	0.059	0.058	90168
B3	0.007	0.007	0.051	0.051	55987
B4	0.007	0.007	0.053	0.057	58000
C1	0.013	0.013	0.037	0.017	74489
C2	0.014	0.008	0.056	0.028	54729
C3	0.007	0.003	0.056	0.025	51317

3.1. Mass accretion rates onto binary black holes

We first show in Figure 2 the orbital phase dependence of mass accretion rates for all models. Through this paper, the mass accretion rate is calculated by counting the number of SPH particles entering the accretion radius of each black hole per unit time. Each mass accretion rate is folded on the orbital period over $40 \leq t \leq 60$. For eccentric binaries (Models B1–C3), the binary is at the periastron (or at the apastron) at phase 0.0 (0.5). For clarity, we vertically offset the mass accretion rates for Model A1 and B1 by +0.3, for Models A2, B2, and C1 by +0.2, and for

Models A3, B3, and C2 by +0.1 with respect to those of Models A4, B4, and C3, respectively.

Hayasaki et al. (2007) already studied the aligned disk case (i.e., $\beta = 0$) corresponding to Model A1. Since the mass continuously falls onto the binary from the circumbinary disk, there is no remarkable orbital-phase dependence in a circular orbit. As a result, no periodic variations are produced in neither mass accretion rates onto the two black holes nor the luminosity of accretion disks surrounding the two black holes. In other words, the accretion proceeds in a quasi-steady fashion, and, hence, no large light variations but small amplitude, random fluctuations are observed. More details are seen in Figures 2, 4 and 8 of Hayasaki et al. (2007). We should note, however, that even in the case of a circular binary, periodic variations may be produced by the formation of spiral patterns excited on the circumbinary disk (MacFadyen & Milosavljević 2008; Daniel et al. 2012). Such features never appear in our calculations with limited spatial dimension of the circumbinary disk and, so, will be explored in future.

The situations differ markedly, if the circumbinary disk is misaligned with respect to the binary orbital plane. In Models A2 and A3, the circumbinary disks are tilted by $\beta = \pi/6$ and $\pi/4$, respectively, while γ is kept the same (i.e., $\gamma = \pi/2$). Both models produce mass-accretion-rate variations with (more than) two peaks in one orbital period, as shown in the left panel of Figure 2. This can be understood in terms of the geometrical effect. In these misaligned systems, two black holes stay away from the circumbinary disk plane in most of time, but twice per orbital period they cross the circumbinary disk plane. Thus, there are two chances in one orbital period that black holes approach the inner region of the circumbinary disk and strip gas from the circumbinary disk. This effect makes the mass accretion rates enhanced around the phases of 0.0 and π . In addition, there are two minor peaks in the mass accretion rate of Model A2. Their origin is, however, unclear at this moment.

We also examine how the mass-accretion-rate variations depend on the azimuth of tilt (γ) in Model A4, in which we assign $\gamma = 0$, keeping other parameters the same as those in Model A2. The resultant variation patterns of the mass accretion rate is the same as those in Model A2 but with a horizontal shift by $\pi/4$, as is expected.

In Models B1–B4, more clear-cut periodic light variations in mass accretion rates are obtained as a natural consequence of the eccentric binary orbit with $e = 0.5$. The coplanar case (i.e., Model B1) was also studied by Hayasaki et al. (2007), who found that binary SMBHs periodically emit intense pulses as a result of the periodic interaction between the binary and the circumbinary disk. The pulse period is therefore the orbital period. The variation amplitude is estimated to be a factor of 6–7 for Models B1 and B2, while it is a factor of 3–4 for Model B3 and B4. Obviously, interactions are strongest when the black holes are at the apastron, where the black holes are closest to the inner edge of the circumbinary disk. However, the mass accretion rate reaches a peak not at the phase $\phi \sim \pi$ (near apastron passage) but at $\phi \sim 0.0$ (near periastron passage). This is because it takes about half an orbital period for the gas stripped from the circumbinary disk to freely fall onto the black holes. In Model B4, we assign $\gamma = 0$, keeping other parameters the same as those in Model B2. The resultant mass accretion rate has a single peak per binary orbit, and the variation amplitude is smaller than that of Model B2. It is interesting to note that double-peak nature, which was observed in Models A2 and A3, is no longer noticeable in Models B2–B4. This is because the effect of orbital eccentricity is stronger than both the misalignment effect and the rotation effect in the azimuth direction, thus erasing the double-peak nature (see section 4). Note that it seems that the mass-accretion-rate variations have a double peaked structure at $\phi \sim 0$ in Model B2 and B3, but such a structure may be numerical artifacts.

We finally performed simulations of Models C1–C3 to see what variations in mass accretion rates are produced by the binary with different masses. The results are shown for Models C1–C3 in the right panel, where the solid line and dashed (red) line represent the mass accretion rates onto the primary and secondary black holes, respectively. Single peaked light variations are obtained for these models. The mass accretion rate onto the secondary black hole is slightly smaller than those onto the primary black hole. Remarkably, the peak phases slightly differ among the two black holes. This is understood as follows. The gas in the inner edge of the circumbinary disk is tidally stripped at the apastron when the secondary black hole gets closest to the circumbinary disk. The gas freely infalls onto the binary while sneaking around the secondary black hole. While a part of the gas accretes at around the periastron onto the primary black hole moving around the center of mass of the binary system, another part of the gas accretes onto the secondary black hole at the periastron passage. The resultant superposed light curve exhibit one double-peaked flare per binary orbit, and its interval between peaks is shorter than those in Models A2, A3, and A4.

3.2. Accretion flow patterns

In order to visualize how gas accretion onto binary SMBHs occurs, we show in Figure 3 sequences of surface density contours for Model A2 (upper panels) and Model B2 (lower panels) at four different phases; at the phases of $t = 59.0$, 59.25, 59.5, and 59.75 from the left to the right, respectively. These panels are illustrated in the inertial frame, and both of the black holes and the circumbinary disk are rotating in the counterclockwise direction. Note that the black holes are rotating more rapidly than the gas in the circumbinary disk according to the Kepler’s third law. The two small points represent the locations of the primary black hole and secondary black hole, respectively. The solid small circles surrounding them represent their accretion radii, which are set to be $r_{\text{acc}} = 0.1a$ from the center of each black hole. The dashed circles in both models represent the inner edge of circumbinary disk $\sim 1.68a$ for Model A2 and the 1:3 outer Lindblad resonance radius $\sim 2.1a$ for Model B2 (see Artymowicz & Lubow 1994), respectively. These density

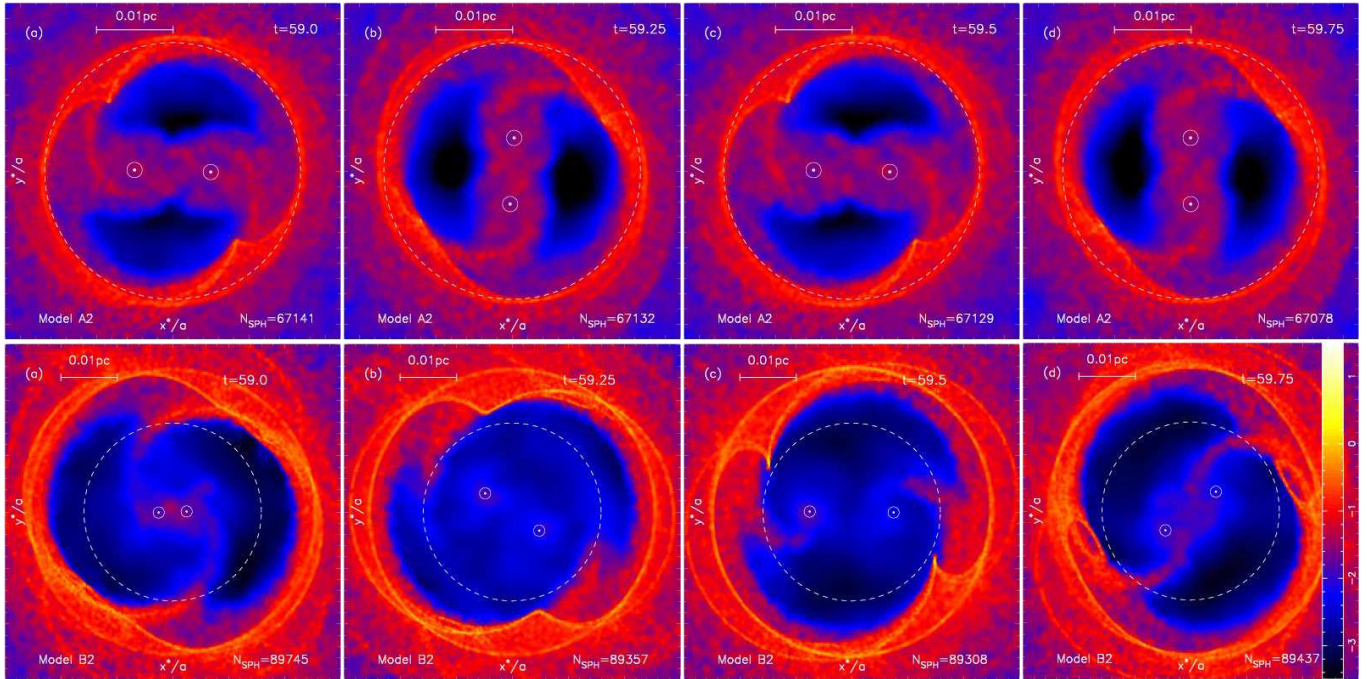


Fig. 3. A sequence of snapshots of the accretion flow from a circumbinary disk onto binary SMBHs in Model A2 (upper four panels) and Model B2 (lower four panels). The color contours of surface density are displayed in the chronological order from the left (a) to the right (d) for each model. The surface density is calculated by integrating density in the direction of the circumbinary disk plane. The two small points and solid circles denote the positions of two black holes and the accretion radii surrounding them, respectively. The figure is shown in the inertial frame; i.e., both of the binary and the circumbinary disk are rotating around the center in the anti-clockwise direction. Note that the disk plane is tilted by $\beta = \pi/6$ from the binary orbital plane with $\gamma = \pi/2$ in both models. The density levels of each panel can be seen in the color chart ($-3.5 \leq \log \Sigma \leq 1.5$) at the right side of lower panel (d). The dashed circle represents the initial inner-edge radius $r_{\text{in}} = 1.68a$ for Model A2, while it is the 1:3 outer Lindblad resonance radius $\sim 2.1a$ for Model B2. Annotated in each panel are the major scale in units of 0.01pc, time in units of P_{orb} , and the number of SPH particles N_{SPH} , respectively.

maps are projected to the circumbinary disk plane (denoted as the x^*-y^* plane).

First, we describe the case of Model A2 (upper panels). Although the flow patterns shown in the upper four panels look quite similar to those in Model A1 reported by Hayasaki et al. (2007), we notice some differences between them. At the elapsed time of $t = 59.0$ and 59.5 as shown in panels (a) and (c), the innermost part of the circumbinary disk is most strongly distorted by the tidal force of each black hole, and therefore the surface density of the innermost part of the circumbinary disk is enhanced at the two positions of $\sim 3\pi/4$ and $\sim 7\pi/4$ from the x^* axis, where cusp structures are observed. This is because each black hole is located within the circumbinary disk plane at those times. By contrast, at the elapsed time of $t = 59.25$ and 59.75 as shown in panels (b) and (d), the cusp density structure disappears, though density enhancements are seen to some extent. This is because each black hole is most distant from the circumbinary disk plane. Now we understand that the time variations of the overall density distribution repeat every half orbital period, which is the period of the passage of the black holes across the circumbinary disk plane. This is responsible for the double-peaked variations in the mass accretion rates.

Let us, next, examine the case of Model B2, which is illustrated in the lower four panels in Figure 3. At the phase of $t = 59.25$ as shown in panel (b), the separation between the two black holes is going to increase and, hence, black holes are approaching the inner edge of the circumbinary disk. At $t = 59.5$ the binary separation reaches its maximum and the distance to the circumbinary disk is at minimum (see panel (c)). The gas in the innermost part of the circumbinary disk is pulled out by the black hole from $t = 59.25$ to 59.5 , thereby a tidal tail being formed and extending inward from the innermost part of the circumbinary disk. This tidal tail continuously grows, and at the phase of $t = 59.75$ as shown in panel (d) we see a bridge connecting the two tidal tails extending from the opposite sides of the circumbinary disk. Gas is supplied to the black hole in a next moment, which is clearly seen in panel (a). In fact, it takes about a half of binary period for gas to fall onto the black holes from the inner edge of the circumbinary disk. This is the reason why mass accretion rate reaches its maximum value at around phase zero. It should be noted that such a gas dynamical behavior is very similar to that in Model B1, which was reported previously (Hayasaki et al. 2007). In other words, the effects of the tilt angle β is not so appreciable for high eccentricity cases. We will discuss why it is so in section 4.

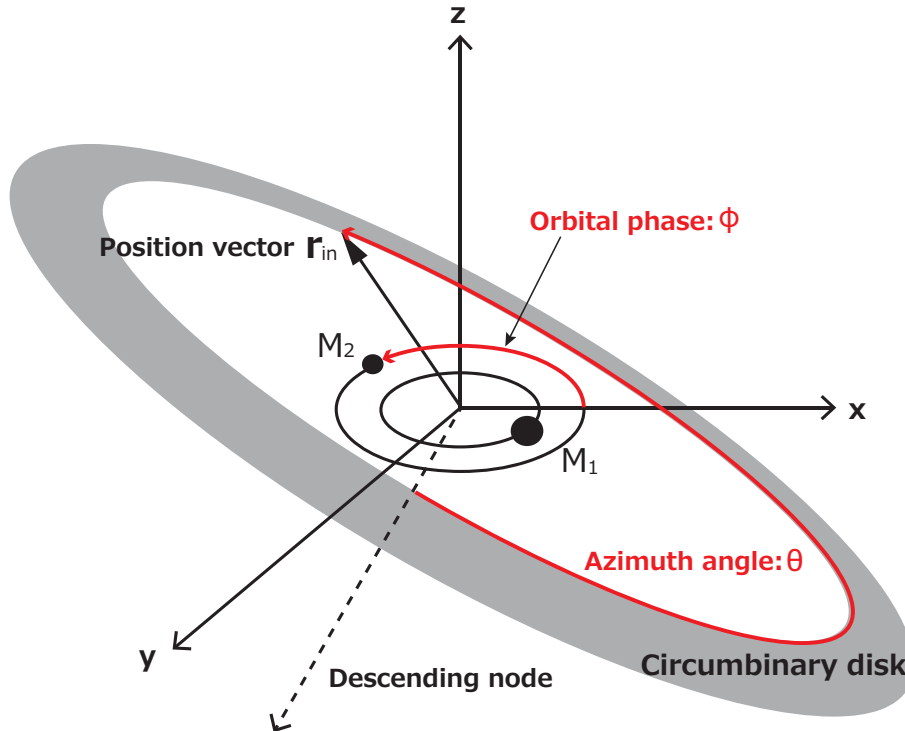


Fig. 4. Schematic view explaining the definitions of the two angles (ϕ, θ) and the descending node. The orbital phase ϕ and the azimuth angle θ are measured from x -axis and the descending node, respectively.

3.3. Averaged mass accretion rates and circularization radii

In Table 3, we summarize the averaged mass-accretion rates and averaged circularization radii around black holes, and the number of SPH particle at the end of run for all models, where the circularization radius, $r_{c,i}$, is defined by $r_{c,i} = j_i^2/GM_i$, [$i = 1, 2$] and j_i represents the specific angular momentum of the SPH particles which enter inside each accretion radius. Thus, their specific angular momentum is proportional to $1/2$ power of circularization radius.

It is noted from Table 3 that the same amount of mass injection is assumed for Models A1–A4, but the nevertheless the averaged accretion rate is higher in Model A1 than others. These trends are also seen in Models B and C.

The averaged circularization radii are about two orders of magnitude larger than the Schwarzschild radius corresponding to each black hole mass. This suggests that the averaged circularization radius of infalling material indicates the size of an accretion disk formed around each black hole. We also note that the averaged circularization radii for the case of $\beta \neq 0$ is larger than those for the case of $\beta = 0$ in all models. This is because the distance between each black hole and its nearest inner edge of the circumbinary disk is longer in the misaligned system ($\beta \neq 0$) than that of the coplanar system ($\beta = 0$). The mass tidally stripped from the circumbinary disk does not directly accrete onto each black hole but via the accretion disk around each black hole. We will briefly discuss how the accretion disk evolve in section 5.

4. Simple semi-analytical models

To understand in a simpler way how a variety of variation patterns in mass accretion rates arises, we construct a semi-analytical model. Since mass accretion occurs by tidal stripping of gas from the inner edge of the circumbinary disk, and since the gravitational attraction force to the circumbinary disk is strongest when the distance between the black hole and its nearest inner edge of the circumbinary disk is at a minimum, we can guess the number of peaks per orbital period by calculating the minimum distance as a function of the orbital phase for parameter sets of all models.

The position vector of the inner edge of the circumbinary disk, \mathbf{r}_{in} , can be expressed by

$$\mathbf{r}_{in} = (r_{in}[\cos\theta \sin\gamma + \sin\theta \cos\gamma \cos\beta], r_{in}[\sin\theta \sin\gamma \cos\beta - \cos\theta \cos\gamma], -r_{in} \sin\theta \sin\beta), \quad (4)$$

where the orbital phase ϕ and the azimuth angle θ are measured from x -axis and the descending node, respectively (see Figure 4). From equations (2) and (4), we obtain the formula for the distance:

$$d(\beta, \gamma, e, q; \phi) = |\mathbf{r}_{in} - \mathbf{r}_i| = \sqrt{4a^2 + r_i^2 - 4ar_i[\sin\theta \cos(\phi - \gamma) \cos\beta - \cos\theta \sin(\phi - \gamma)]}, \quad (5)$$

where the value of θ for a given ϕ is numerically chosen so as to give the minimum distance. Here, we assign $i = 2$, since the less massive black hole can move on a larger extent, thereby getting closer to the circumbinary disk than the massive one.

Figure 5 shows the orbital phase dependence of the distance between the black hole and its nearest inner edge of circumbinary disk. There are four different parameters: orbital eccentricity (e), mass ratio (q), tilt angle (β), and azimuth of tilt (γ). The dependence of $d(\beta, \gamma, e, q; \phi)$ normalized by the semi-major axis on these parameters are shown in panels (i)-(v). The fiducial parameters are those of Model A2; i.e., $(\beta, \gamma, e, q) = (\pi/6, \pi/2, 0.0, 1.0)$.

Panel (i) shows γ -dependence of normalized distance, $d(\beta, \gamma, e, q; \phi)/a$, for fixed values of $(q, e, \beta) = (1.0, 0.0, \pi/6)$. The solid line, dotted line, dashed line, and dash-dotted line represent $d(\phi)/a$ for $\gamma = \pi/2, 0, \pi/6$, and $\pi/4$, respectively. We note that $d(\phi)/a$ is the shortest twice per binary orbit and that the phases of the minimum distance shift by varying the parameter γ . Here, let us go back to see the difference between mass accretion rate of Model A2 and that of Model A4. The phase difference between the solid line ($\gamma = \pi/2$) and the dotted line ($\gamma = 0$) is $\pi/2$. This supports our simulation results of Models A2 and A4.

Panel (ii) shows β -dependence of the normalized distance for the fixed values of $(q, e, \gamma) = (1.0, 0.0, \pi/2)$. The solid line, dashed line, dash-dotted line, and dotted line represent $d(\phi)/a$ for $\beta = \pi/6, 0, \pi/4$, and $\pi/2$, respectively. The normalized distance reaches its minimum value twice per binary orbital period except for the case with $\beta = 0$, in which $d(\phi)/a$ is constant. That is, the non-zero values of β is essential to produce two peaks per binary orbit in the mass-accretion-rate variations. This panel provides a reasonable explanation about why the results of Models A2-A4 are shown in the left panel of Figure 2.

Panel (iii) shows e -dependence of the normalized distance for the fixed values of $(q, \beta, \gamma) = (1.0, \pi/6, \pi/2)$. The solid line, dashed line, dash-dotted line, dotted line, and three-dotted line represent $d(\phi)/a$ for $e = 0, 0.1, 0.2, 0.3$, and 0.4 , respectively. The normalized distance has two round peaks for $e = 0$, but the larger e is, the deeper becomes a hollow at around $\phi = \pi$. Although we have mentioned that non-zero values of β give rise to the double peaked modulations in mass accretion rates, this is not always the case when the orbital eccentricity is not zero. This will explain that the mass accretion rates of Models B2, B3, and B4 have a single peaked shape. We have also calculated the cases with $\gamma = 0.0$, reaching the same conclusion; i.e., single peaked variations are found for $e \gtrsim 0.3$. This supports the result of Model B4.

Panel (iv) shows q -dependence of the normalized distance between the secondary (less massive) black hole and its nearest inner edge of the circumbinary disk for the fixed values of $(e, \beta, \gamma) = (0, \pi/6, \pi/2)$. The solid line, dashed line, dash-dotted line, dotted line, and three-dotted line represent $d(\phi)/a$ for $q = 1.0, 0.1, 0.3, 0.5$, and 0.7 , respectively. The lower the binary mass ratio is, the shorter becomes $d(\phi)/a$. Variations in the mass ratio do not change the number of peaks of the normalized distance. Obviously, the smaller q is, the smaller becomes the mean distance. This is because the semi-major axis of the secondary black hole (r_2 in equation 3) increases as q decreases.

Panel (v) shows the same γ -dependence as those in panel (i) but for $e = 0.1$. This panel shows how the normalized distance changes with γ for the cases with an even smaller orbital eccentricity. The solid line, dotted line, dashed line, and dash-dotted line represent $d(\phi)/a$ for $\gamma = \pi/2, 0, \pi/6$, and $\pi/4$, respectively. The solid line is the same as the dashed line of panel (iii). It is interesting to note that double peaked variation curve for the case of $\gamma = 0$ changes to a single peaked one as γ increases.

5. Discussion

Periodic light variations are not generally observed from single SMBH systems. There is a report for the presence of quasi-periodic oscillations (QPOs) in AGNs (Gierliński et al. 2008), but the QPOs do not mean periodic occurrence of clear-cut flares but mean rather gradual variations. Unlike single SMBH systems, periodic light variations can be seen in an eccentric binary black hole system because of periodically enhanced binary-disk interactions. In most of previous studies, it was implicitly assumed that the binary orbital plane is aligned with the circumbinary disk plane. Since there are no strong reasons to believe the binary-disk alignment, it is natural to relax this assumption and to examine what light variations are expected for the misaligned system. As shown in Figure 2, a circular binary surrounded by a misaligned circumbinary disk exhibits a double peak structure in the variations of mass accretion rates, whereas an eccentric binary with a moderately large orbital eccentricity shows a single peak per orbit, even if the circumbinary disk is inclined from the binary orbital plane.

5.1. Inner edge radius of misaligned circumbinary disks

The radius of the inner edge of the circumbinary disk is determined by the balance between the viscous torque of the prograde circumbinary disk and the tidal/resonant torque which acts on it (Artymowicz & Lubow 1994). In the case of moderate orbital eccentricity, the typical inner edge radius is at the 1 : 3 outer Lindblad resonance radius, which is estimated to be $\sim 2.1a$. If the circumbinary disk is misaligned with respect to the binary plane, the resonant torque will be weaker than otherwise, which makes the inner edge smaller. In order to more precisely determine the size of the inner edge of the circumbinary disk, we need to investigate how the tidal/resonant torque acts on the misaligned

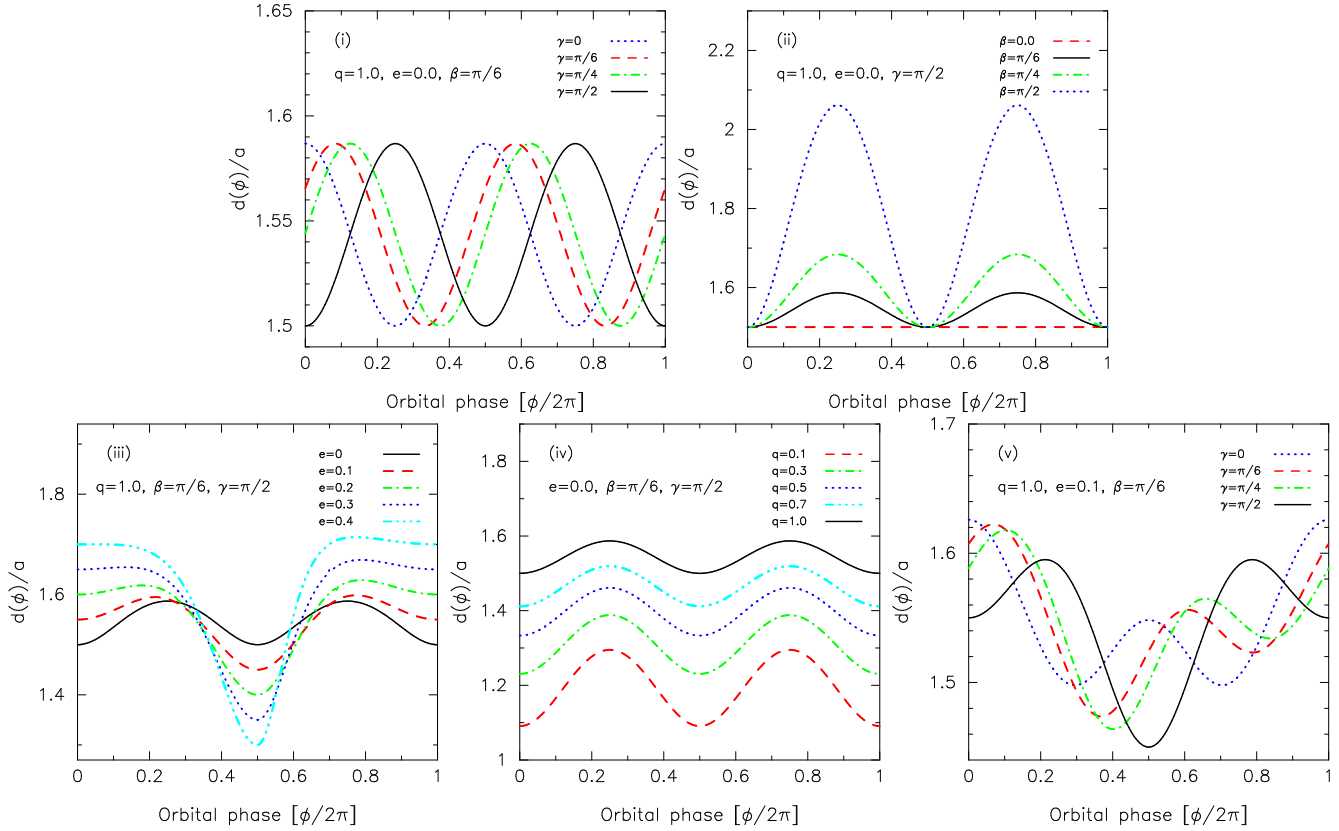


Fig. 5. Orbital phase dependence of the normalized distance, $d(\beta, \gamma, e, q; \phi)/a$, between the black hole and the inner edge of circumbinary disk. The dependence of the normalized distance on the four parameters: β , γ , e , and q are shown in panels (i)–(v). In all the panels, the solid (black) line indicates the fiducial model; $(\beta, \gamma, e, q) = (\pi/6, \pi/2, 0.0, 1.0)$ for panels (i)–(iv) and $(\beta, \gamma, e, q) = (\pi/6, \pi/2, 0.1, 1.0)$ for panel (v). For the meanings of other lines, see text and the explanations in each panel.

circumbinary disk. This is also essential to calculate the circumbinary disk structure.

5.2. Triple disk model for OJ 287

A blazar OJ287 exhibits quasi-periodic optical outbursts of 12 year interval. In order to explain such quasi-periodic nature, a binary black hole model was firstly proposed by (Sillanpää et al. 1988). Lehto & Valtonen (1996) subsequently proposed the modified model that a less massive black hole orbits around a more massive one with undergoing relativistic precession and impacts twice per binary orbit on the accretion disk around the more massive black hole. This model can explain the quasi-periodicity of outbursts with a double peak structure at a few year interval.

As shown in Models C1 and C2 at the right panel of Figure 2, the solid line and dashed (red) line represent the mass accretion rates of the primary black hole and that of the secondary black hole, respectively. Respective mass accretion rates periodically vary with time and have a single peak around the periastron but slightly different orbital phases. The resultant combined mass accretion rate provides a periodic double peaked structure with a short interval. We, therefore, propose an alternative binary black hole model that the circumbinary disk around an eccentric binary composing of black holes with different masses is misaligned by a relatively small tilt angle ($0 \lesssim \beta \lesssim \pi/6$).

5.3. Precessions of misaligned circumbinary disks

The binary-disk interaction also gives rise to a precession of the circumbinary disk (MacFadyen & Milosavljević 2008; Hayasaki & Okazaki 2009; Daniel et al. 2012). With the assumption that $r \gg a$ and $M_2 \ll M_1$, the precession frequency of the misaligned circumbinary disk is given by (e.g., Nixon et al. 2011b) as

$$\frac{P_{\text{prec}}}{P_{\text{orb}}} \approx \frac{4}{3} \frac{1+q}{q} \left(\frac{r}{a}\right)^{7/2} \frac{1}{|\cos\beta|} \quad (-\pi/2 < \beta < \pi/2), \quad (6)$$

where P_{prec} and P_{orb} are the precession period and binary orbital period, respectively. It is clear that P_{prec} is much longer than P_{orb} , e.g. $P_{\text{prec}} \gtrsim 100P_{\text{orb}}$ for $q = 0.1$ and $r = 2a$. This can produce a light variation in circumbinary disk with a beat period P_{beat} , where it is expressed by $1/P_{\text{beat}} \equiv 1/P_{\text{orb}} - 1/P_{\text{prec}}$. From equation (6), we obtain the beat period normalized by the binary orbital period:

$$\frac{P_{\text{beat}}}{P_{\text{orb}}} = \left[1 - \frac{3}{4} \left(\frac{r}{a} \right)^{-7/2} \frac{q}{1+q} |\cos\beta| \right]^{-1} \quad (7)$$

which is slightly longer than the orbital period, as far as $r \gg a$. The beat period for the case of $q = 0.1$ and $r = 2a$ is, for example, approximately $1.01P_{\text{orb}}$. In a subsequent paper, we will study this topic in more detail.

5.4. Luminosity variations

Another interesting topic is how the mass finally accretes onto each black hole via an accretion disk from the circumbinary disk. In section 3.3, we show that the infalling material is circularized around each black hole (the estimated circularization radii can be seen in Table 3). This leads to the formation of the triple disk system, which is composed of two accretion disks around black holes and one circumbinary disk surrounding them (Hayasaki et al. 2008). However, it is poorly known what structure each accretion disk has and how it evolves. Once these two accretion disks are formed by gas supply from the circumbinary disk, they viscously evolve and gas in the accretion disk finally accretes onto each black hole after the viscous timescale. Assuming that the accretion disk is the standard disk, the viscous timescale measured at the circularization radius is much longer than the binary orbital period. The precise shape of light curves may be different from that of variations in mass accretion rates. It is interesting to examine the basic properties of radiations emitted from each accretion disk.

6. Conclusions

We have carried out numerical simulations of accretion flows from a circumbinary disk which is inclined from the binary orbital plane, in order to examine to what extent the basic properties of mass-accretion-rate variations may alter, compared with the coplanar cases. Our main conclusions are summarized as follows:

1. We find that the mass accretion rates exhibit a double peak per binary orbit in a circular binary system, when the circumbinary disk is misaligned with the binary orbital plane. This is because each black hole passes across the circumbinary disk plane twice per binary orbit and then attracts the gas there. This double peak nature of mass accretion rates is also independent of the azimuth of tilt. The tilt angle is one of important orbital parameters to determine variation patterns of radiations emitted from a binary black hole system.
2. The orbital eccentricity remains to be an important orbital parameter to produce single sharply peaked variations per binary orbit in mass accretion rates even in a misaligned circumbinary disk system. This is because each black hole is closest to the inner edge of circumbinary disk once per binary orbit in most cases. The simple semi-analytic model (see section 4) predicts that this single peak nature is independent of both the tilt angle and the azimuth of tilt, as long as $e \gtrsim 0.3$.
3. In the case of an eccentric binary composing of black holes with different masses, the less massive black hole can get closer to the circumbinary disk than the massive one, thus tidally splitting gas from its inner edge, but the created gas flows are comparably captured by both black holes with a short time delay. The superposed accretion rates show periodic outbursts with an apparent double peaked structure with a short interval.

KH thanks Atsuo T. Okazaki for helpful suggestions. The numerical simulations reported here were performed using the computer facilities of Yukawa Institute of Theoretical Physics, Kyoto University. This work is supported in part by the Grants-in-Aid of the Ministry of Education, Science, Culture, and Sport and Technology (MEXT) [21540304, 22340045, 22540243, 23540271 KH, 22340045 SM], and the global COE programs on The Next Generation of Physics, Spun from Diversity and Emergence from MEXT.

References

- Amaro-Seoane, P., et. al 2012, arXiv:1201.3621
 Armitage, P. J., & Natarajan, P. 2002, ApJ, 567, L9
 Artymowicz, P., & Lubow, S.H. 1994, ApJ, 421, 651
 Artymowicz, P., & Lubow, S.H. 1996, ApJ, 467, L77
 Bate, M. R., Bonnel, I. A., & Price, N.M. 1995, MNRAS, 277, 362
 Benz W. 1990, in the Numerical Modeling of Nonlinear Stellar Pulsations: Problems and Prospects, ed. Buchler, R.J. (Dordrecht: Kluwer Academic Publishers), 269
 Benz, W., Bowers, R.L., Cameron, A.G.W., & Press, W.H. 1990, ApJ, 348, 647
 Begelman, M. C., Blandford, R. D., & Rees, M. J. 1980, Nature, 287, 307
 Bode, T., Haas, R., Bogdanović, T., Laguna, P., & Shomarker, D. 2010, ApJ, 715, 1117
 Bode, T., Bogdanović, T., Haas, R., Healy, J., Laguna, P., & Shoemaker, D. 2012, ApJ, 744, 1
 Bogdanović, T., Smith, B. D., Sigurdsson, S., & Eracleous, M. 2008, ApJ, 174, 455
 Bogdanović, T., Eracleous, M., & Sigurdsson, S. 2009, ApJ, 697, 288
 Boroson, T. A., & Lauer, T. R. 2009, Nature, 458, 53
 Chang, P., Strubble, L.E., Menou, K., & Quataret, E. 2010, MNRAS, 407, 2007
 Cuadra, J., Armitage, P.J., Alexander, R.D., & Begelman, M.C. 2009, MNRAS, 393, 1423
 DfOrazio, J. D., Haiman, Z., & MacFadyen, A. arXiv:1210.0536
 Dotti, M., Colpi, M., Haardt, F., Mayer, L. 2007, MNRAS,

- 379, 956
- Dotti, M., Montuori, C., Decarli, R., Volonteri, M., Colpi, M., & Haardt, F. 2009, *MNRAS*, 398, L73
- Elacleous, M., Boroson, T. A., Halpern, J. P., & Liu, J. 2012, *ApJS*, 201, 23
- Escala, A., Larson, R. B., Coppi, P. S., & Mardones, D. 2005, *ApJ*, 630, 152
- Farris, B. D., Liu, Y. T., & Shapiro, S. L. 2011, *Phys. Rev. D*, 84, 024024
- Farris, B. D., Gold, R., Paschelidis V., Etienne Z. B., & Shapiro, S. L. 2012, arXiv:1207.3354
- Gaskell, C. M. 1996, *ApJ*, 464, L107
- Gould, A., & Rix, H. W. 2000, *ApJ*, 532, L29
- Gebhardt, K., et al. 2000, *ApJL*, 539, L13
- Gierliński M., Middleton M., Ward M., & Done C. 2008, *Nature*, 455, 369
- Ferrarese, L., & Merritt, D. 2000, *ApJL*, 539, L9
- Haiman, Z., Kocsis, B., & Menou, K. 2009, *ApJ*, 700, 1952
- Hayasaki, K., Mineshige, S., & Ho, C. L. 2008, *ApJ*, 682, 1134
- Hayasaki, K., Mineshige, S., & Sudou, H. 2007, *PASJ*, 59, 427
- Hayasaki, K. 2009, *PASJ*, 61, 65
- Hayasaki, K., & Okazaki, A.T. 2009, *ApJ*, 691, L5
- Hayasaki, K., Ueda, Y., & Isoe, N. 2010, *PASJ*, 62, 1351
- Hayasaki, K. 2011, *ApJ*, 2011, 726, L14
- Hayasaki, K., Yagi, K., Tanaka, T., & Mineshige, S. 2012, arXiv:1201.2858
- Iguchi, S., & Sudou, H. 2010, *ApJ*, 724, L166
- Ivanov, P. B., Papaloizou, J. C. B., Polnarev, A. G. 1999, *MNRAS*, 307, 79
- Kato, S., Fukue, J., & Mineshige, S. 2008, *Black-Hole Accretion Disks, Towards a New Paradigm* (Kyoto: Kyoto University Press)
- Kocsis, B., Haiman, Z., & Loeb, A. arXiv1205.4714
- Kocsis, B., Haiman, Z., & Loeb, A. arXiv1205.5268
- Kocsis, B., Yunes, N., & Loeb, A. 2011, *Phys. Rev. D*, 84, 024032
- Komossa, S., Burwitz, V., Hasinger, G., Predehl, P., Kaastra, J. S., Ikebe, Y. 2003, *ApJ*, 582, L15
- Komossa, S. 2006, *Mem. Soc. Astron. Ital.*, 77, 733
- Lehto, H. J., & Valtonen, M. J. 1996, *ApJ*, 460, 207
- Lobanov, A. P., & Roland, J. 2005, *A&A*, 431, 831
- Lodato G., Nayakshin S., King A. R., Pringle J. E., 2009, *MNRAS*, 398, 1392
- MacFadyen, I.A., & Milosavljević, M. 2008, *ApJ*, 672, 83
- Magorrian, J., et al. 1998, *AJ*, 115, 2285
- Murray C.D., Dermott S.F., 1999, *Solar System Dynamics* (Cambridge: Cambridge University Press), ch.2, pp26-28
- Mayer, L., Kazantzidis, S., Madau, P., Colpi, M., Quinn, T., Wadsley, J., 2007. *Science*, 316, 1874
- Milosavljević, M., & Phinney, E.S. 2005, *ApJ*, 622, L93
- Merritt, D., & Ekers, R. D. 2002, *Science*, 297, 1310
- Mošta, P., Palenzuela, C., Rezzolla, L., et al. 2010, *Phys. Rev. D*, 81, 064017
- Montuori, C., Dotti, M., Colpi, M., Decarli, R., Haardt, F. 2011, *MNRAS*, 412, 26
- Montuori, C., Dotti, M., Colpi, M., Decarli, R., Haardt, F. 2012, *MNRAS*, 425, 1633
- Nixon, C. J., Cossins, P.J., King, A. R., & Pringle, J.E. 2011, *MNRAS*, 412, 1591
- Nixon, C. J., King, A.R., & Pringle, J.E. 2011, *MNRAS*, 417, L66
- Nixon, C. J. 2012, *MNRAS*, 423, 2597
- Noble, S. C., Mundim, B. C., Nakano, H., Krolik, J. H., Campanelli, M., Zlochower, Y., & Yunes, N. 2012, *ApJ*, 755, 51
- Okazaki, A. T., Bate, M. R., Ogilvie, G. I., & Pringle, J. E. 2002, *MNRAS*, 337, 967
- Okazaki, A. T., Nagataki, S., Naito, T., et al. 2011, *PASJ*, 63, 893
- Pringle, J. E. 1996, *MNRAS*, 281, 357
- Papaloizou, J., & Pringle, J. E. 1977, *MNRAS*, 181, 441
- Palenzuela, C., Lehner, L., & Liebling, S. L. 2010, *Science*, 329, 927
- Rodriguez, C., Taylor, G. B., Zavala, R. T., Peck, A. B., Pollack, L. K., & Romani, R. W. 2006, *ApJ*, 646, 49
- Roedig, C., Dotti, M., Sesana, A., Cuadra, J., & Colpi, M. 2011, *MNRAS*, 415, 3033
- Sesana, A., Roedig, C., Reynolds, M. T., & Dotti, M. 2012, *MNRAS*, 420, 860
- Shi, Ji-M, Krolik, J. H, Lubow, S. H., & Hawley, J. F. 2012, *ApJ*, 749, 118
- Shakura, N. I., & Sunyaev, R. A. 1973, *A&A*, 24, 337
- Sillanpää, A., Haarala, S., Valtonen, M. J., Sundelius, B., & Byrd, G. G. 1988, *ApJ*, 325, 628
- Sudou, H., Iguchi, S., Murata, Y., & Taniguchi, Y. 2003, *Science*, 300, 1263
- Takata, J., Okazaki, A. T., Nagataki, S., Naito, T., Kawachi, A., Lee, S.-H., Mori, M., Hayasaki, K., Yamaguchi, M. S., & Owocki, S. P. 2012, *ApJ*, 750, 70
- Tanaka, T., & Menou, K. 2010., *ApJ*, 714, 404
- Tanaka, T., Menou, K., & Haiman, Z. 2012, *MNRAS*, 420, 705
- Valtonen, M. J., Lehato, J. H., Takalo, L. O., & Sillanpää, A. 2011, *ApJ*, 729, 33
- Yokosawa, M., & Inoue, M. 1985, *PASJ*, 37, 655
- Yunes, N., Kocsis, B., Loeb, A., & Haiman, Z. 2011, *Phys. Rev. Lett.*, 107, 171103